STUDY OF ENHANCED BOILING HEAT TRANSFER BY MICRO-STRUCTURE SURFACES WITH HYDROPHILIC-HYDROPHOBIC COMBINED

by

Qingsuo GUO, Zhiming WANG, Wenshan QIN, and Fei DONG*

School of Automotive and Traffic Engineering, Jiangsu University, Zhenjiang, China

Original scientific paper
https://doi.org/10.2298/TSCI230225129G

The VOF model was employed to simulate the pool boiling under typical engine-operating temperature conditions and was experimentally validated. A trapezoidal raised surface morphology with a hydrophilic-hydrophobic combination was designed, and the heat transfer ability and bubble evolution phenomena on the surface were analyzed. Then the variance contribution of each structural parameter of the trapezoidal raised surface to the average surface temperature rise and the average surface heat transfer was evaluated. Finally, the NSGA-II algorithm was used to optimize the structural design of the designed trapezoidal raised surface with the optimization objectives of minimizing the average temperature rise and maximizing the average heat transfer coefficient. Specifically, compared with the hydrophilic smooth surface, the optimized structure showed an increase in the average heat transfer coefficient by 194.5% and a decrease in the maximum average temperature rise, ΔT, by 33.9%.

Key words: *hydrophilic-hydrophobic combination, structure optimization, enhanced heat transfer, micro-structure surface*

Introduction

Modern internal combustion engines are continuously advancing towards higher power, lighter weight, and smaller size, which presents significant challenges to engine design and development [1-3]. Increasing the cooling efficiency of internal combustion engines is essential for improving their performance and reliability. By improving the cooling efficiency, the engine can operate at higher temperatures and pressures, resulting in increased power output and improved fuel efficiency [4-6]. Boiling heat transfer has been widely applied in improving the cooling efficiency of internal combustion engines due to its advantages such as high heat transfer efficiency and self-stabilization. [7, 8].

Bova *et al.* [9] conducted experiments on a low flow rate cooling engine, and the results showed that nucleate boiling was formed, thus improving the efficiency of engine cooling and reducing the power consumption of the pump. Torregrosa *et al.* [10, 11] employed aluminum rectangular horizontal runners to simulate heat transfer conditions at low flow rates in engines, with calculated heat flow density in the heat transfer direction. By utilizing a high speed camera to acquire microscopic properties on the heated surface, they provided the foundation for bubble dynamics model corrections. Hua *et al*. [12] simulated the two-phase flow boiling heat transfer characteristics inside the actual internal combustion engine water jacket, obtaining

* Corresponding author, e-mail: jsdxdf@163.com

highly accurate temperature distribution in the cylinder head and flow field diagrams of the gas phase and cooling water chamber.

A lot of research has been done on how to enhance boiling heat transfer, especially in terms of structural changes. Jafari *et al.* [13] simulated the entire process of vapor bubble growth from the pits to detachment on the surface of the pits inside the micro-channel, and their findings demonstrated that the surface with pits was able to enhance the boiling heat transfer capacity by a factor of eight compared to a smooth plane. Dong *et al*. [14] conducted a saturated pool boiling experiment using a heating surface with micro-structures. The research found that micro-structures can promote bubble nucleation and increase the density of active nucleation sites, especially at low heat flux densities. This enhances the boiling heat transfer effect.

The wall wettability has also garnered the attention of numerous scholars due to its distinctive phase change heat transfer characteristics. Phan *et al*. [15] conducted pool boiling experiments on seven surfaces with contact angles ranging from 22°-112°. The results revealed that the smaller the contact angle, the smaller the bubble detachment diameter, the higher the detachment frequency, and the better the heat transfer performance. Beta *et al.* [16] used a superhydrophilic surface as a substrate on which a surface structure with spaced hydrophobic points was arranged. The results showed that the nucleated boiling heat transfer coefficient (HTC) and critical heat flow density of this surface were enhanced by 65% and 100%, respectively, compared to the hydrophilic surface. Li *et al.* [17] used lattice Boltzmann numerical simulation method to study the pool boiling process on a hydrophilic-hydrophobic mixed surface with micro pillar structures. The research found that the hydrophobicity on the top of the pillars can reduce the wall superheat at the boiling incipience, but it can also cause the boiling process to enter the film boiling state at lower wall superheat.

This study found that setting the top of the trapezoidal raised micro-structure surface to be hydrophobic can accelerate the detachment speed of bubbles from the heat transfer surface, reduce the detachment diameter, and promote the heat transfer rate of bubbles. This ultimately results in lower temperature rise on the heat exchange surface and a higher HTC. By utilizing this property, we used the response surface method to obtain the impact of various structural variables on the surface heat transfer capability. It was found that the height of trapezoidal protrusions was the factor that had the greatest impact on improving the boiling heat transfer capability. Finally, with the research objectives of minimizing the average temperature rise and maximizing the HTC, we optimized the micro-structure design and successfully obtained the optimal solution.

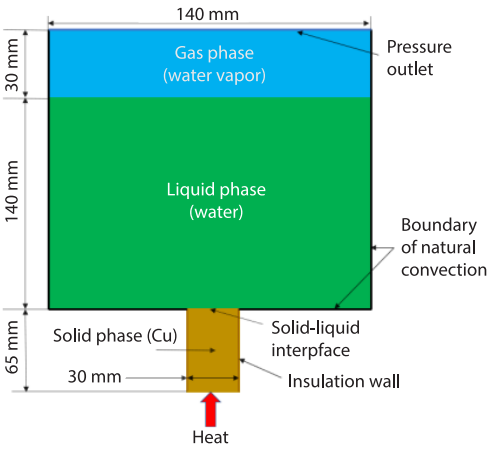

Figure 1. Geometry model of pool boiling system

Model building

Initial geometric model

The depicted 2-D pool boiling model, as shown in fig. 1, utilizes a copper block as the solid phase, water as the liquid phase, and water vapor as the gas phase. The bottom of the copper block is the heat input location and the top of the gas phase is the pressure outlet. Natural convective heat exchange takes place when air comes in contact with the walls of the gas and liquid phases, while the walls of the solid sides

are set to be insulated. During the calculation, the physical properties of the material are set as constants and set according to the specific values in tab. 1. At the same time, the influence of gravity is considered.

Table 1. Physical properties of each material

Material	Density [kgm^{-3}]	Viscosity [kgm^{-1}s^{-1}]	Thermal conductivity [Wm^{-1}K^{-1}]	Specific heat capacity [Jkg^{-1}K^{-1}]
Water	1000	0.0003	0.6	4182
Water vapor	0.5542	$1.34 \cdot 10^{-5}$	0.0261	2014
Copper	8960	–	387.6	381

Governing equation

In this paper, we employed FLUENT as the computational software and the model utilized the VOF model. The model can conveniently identify the position of each phase interface in a multi-phase flow, thus enabling it to be utilized in this paper for the investigation of bubble motion behavior. The set of control equations:

– Continuity equation

$$\frac{\partial \alpha_l}{\partial t} + \nabla\left(\alpha_l \vec{\mathrm{v}}\right) = -\frac{S}{\rho_l} \tag{1}$$

$$\frac{\partial \alpha_v}{\partial t} + \nabla\left(\alpha_v \vec{\mathrm{v}}\right) = \frac{S}{\rho_v} \tag{2}$$

– Momentum equation

$$\frac{\partial}{\partial t}\left(\rho \vec{\mathrm{v}}\right) + \nabla\left(\rho \vec{\mathrm{v}}\vec{\mathrm{v}}\right) = -\nabla\rho + \nabla\left[\mu\left(\nabla\vec{\mathrm{v}} + \nabla\vec{\mathrm{v}}^T\right)\right] + \rho\vec{\mathrm{g}} + \vec{\mathrm{F}} \tag{3}$$

– Energy equation

$$\frac{\partial}{\partial t}\left(\rho E\right) + \nabla\left[\vec{\mathrm{v}}\left(\rho E + p\right)\right] = \nabla\left(k\nabla T\right) + Q \tag{4}$$

where α_l is the volume fraction of the water, α_v – the volume fraction of the vapor, $\vec{\mathrm{v}}$ – the velocity, S – the source term of the mass at the phase transition, $\vec{\mathrm{F}}$ – the volume force, T – the temperature, p – the local pressure, and Q – the energy source term during the phase transition. The remaining parameters (kinetic viscosity, μ, density, ρ, thermal conductivity, k, and internal energy, E) are obtained as a weighted average of the gas and liquid phases.

The volume force $\vec{\mathrm{F}}$ generated by the surface tension in the momentum equation is derived from the continuous surface force model:

$$\vec{\mathrm{F}} = \sigma_l \frac{\rho\delta_l \nabla\alpha_l}{0.5\left(\rho_l + \rho_v\right)} \tag{5}$$

$$\delta_l = \nabla\nabla\alpha_l \tag{6}$$

where σ_l is the surface tension coefficient and δ_l – the liquid phase curvature.

The mass source term and the energy source phase of the phase change process are obtained from the following equation:

$$S = \begin{cases} \tau\alpha_v\rho_v \dfrac{T_L - T_{\text{sat}}}{T_{\text{sat}}} & T_L \geq T_{\text{sat}} \\ \tau\alpha_v\rho_v \dfrac{T_L - T_{\text{sat}}}{T_{\text{sat}}} & T_L < T_{\text{sat}} \end{cases} \tag{7}$$

$$Q = -h_{lv} S \tag{8}$$

where τ [3s^{-1}] is the adjustment factor, h_{lv} – the latent heat of vaporization, T_L – the liquid phase temperature of the heat transfer medium, and T_{sat} – the liquid saturation temperature.

The numerical simulations in this paper employed the SIMPLE algorithm. The geometric reconstruction method (geo-re-construct) is chosen for the discrete format of VOF. Solve the equations of energy and momentum using the second-order upwind format. The PRESTO! solves the pressure.

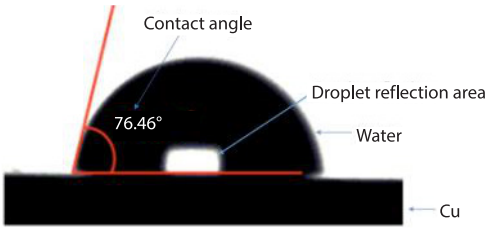

Figure 2. Copper block surface contact angle measurement results

Boundary conditions

The initial temperatures of the liquid and solid phases are set to 80 °C, which corresponds to the cooling system temperature during normal engine operation. Heat is introduced into the calculation domain from the bottom of the solid phase, while the top of the gas phase is defined as a pressure outlet with a pressure level of one atmosphere. The convective HTC of the surface with natural-convection of air is set to 5 W/m^{2}K. Figure 2 shows the results of the contact angle size measurements, with the white part of the droplet center in the image being the reflected led light.

It is considered that the surface tension varies with temperature and has a strong influence on the growth and movement of bubbles. Therefore, the surface tension should be corrected for the temperature change [18]. This is given by the following equation.

$$\sigma = 0.09537 - 2.24 \cdot 10^{-6} T - 2.56 \cdot 10^{-7} T^2 \tag{9}$$

Grid independence

To ensure accuracy and reduce calculation time, the appropriate grid size must be determined. The wall superheat on the upper surface of the copper block in this section is used as the evaluation criterion for the grid irrelevance study, as shown in tab. 2. As the grid number increases, the wall superheat gradually stabilizes, and the values are equal at 0.1 mm and 0.2 mm. Therefore, the final grid size scheme of 0.2 mm is selected.

Table 2. Grid independence calculation results

Grid solution	Grid size [mm]	Number of mesh	Wall of superheat [°C]
1	0.5	103571	21.1
2	0.4	162019	22.5
3	0.3	286986	23.8
4	0.2	649570	24.6
5	0.1	2577210	24.6

Experimental verification

The pool boiling heat transfer experimental rig constructed is illustrated in fig. 3. This device is comprised of three main components: a heating system that features copper block and heating rods equipped with voltage regulator. A temperature control system, including cooling water, auxiliary heater and a temperature controller. A data acquisition system with integrated thermocouple, temperature monitoring and logger.

Figure 4 shows the external 3-D view and vertical sectional view of the copper block. Thermocouples are mounted at positions A and B. Nine heating rods are arranged in the heating holes on the bottom side of the copper block to ensure uniform heat transfer in the vertical direction. Aluminum silicate material was used to insulate the copper block to reduce heat loss.

During the experiment, deionized water is first heated to 80 °C using an auxiliary heater. The auxiliary heater is set to auto-heat mode and will turn on automatically if the temperature falls below 80 °C. If the system temperature rises above 80 °C, cooling water will be imported to take away any excess heat. Turn on the voltage regulator, input heat to the system, and wait for the system temperature to stabilize before recording the temperature value. To reduce the impact of environmental errors, it is necessary to record five sets of data and take the average value. Gradually increase the voltage by 10 V increments until it reaches 380 V, and repeat the temperature recording procedure, documenting the temperature reading at each voltage level. In addition, to consider the influence of calculation and measurement errors on the experimental results, we conducted an uncertainty analysis of the wall temperature and HTC, with detailed results shown in tab. 3.

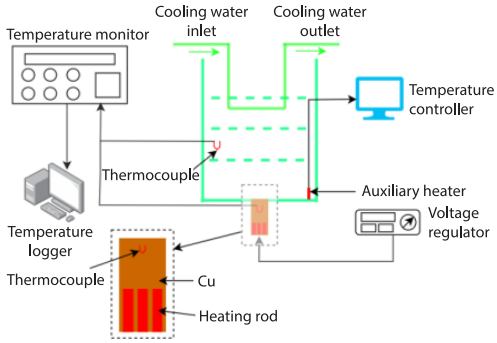

Figure 3. Diagram of the experimental system

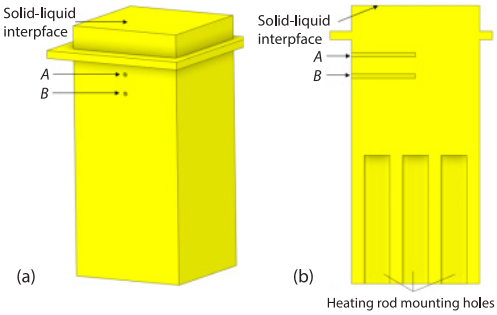

Figure 4. Schematic diagram of the structure of a copper block; (a) external 3-D view of the copper block and (b) vertical sectional view of the copper block

Table 3. Uncertainty analysis results

	Accuracy	Uncertainty	
		Temperature	HTC
Temperature controller	±0.5 °C	±0.7 °C	<3%
Temperature monitor	±0.1°C		
Thermocouple	±0.1°C		

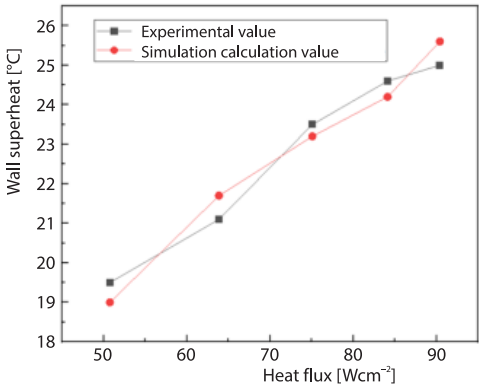

Figure 5. Comparison of experimental and simulation results

In the simulation calculation, the initial temperature of the liquid phase and solid phase is set to 80 °C, and the external atmospheric temperature is set to room temperature of 25 °C. Figure 5 displays the experimental and simulated values of wall superheat for various heat flux conditions. It can be observed that the relative error between the experimental and simulated values of wall superheat is minimal, with the highest error occurring at a heat flux of 63.86 W/cm^2, which is only 2.76%. Therefore, the established numerical calculation simulations are considered to be accurate.

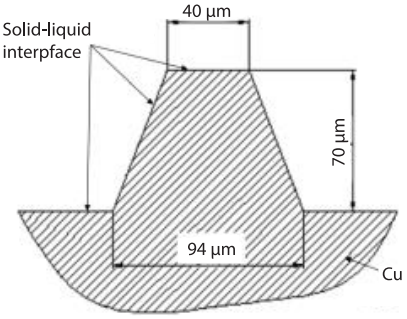

Figure 6. Schematic diagram of trapezoidal raised structure

Micro-structured surface solution design

To improve boiling heat transfer using micro-structured surfaces, a trapezoidal raised structure was designed, as shown in fig. 6. Two wettability schemes were designed at the solid-liquid interface with a trapezoidal raised structure, as shown in fig. 7. Scheme 1, set the contact angle at the solid-liquid interface to 35° to exhibit hydrophilicity, as shown in fig. 7(a). Scheme 2 uses a hydrophilic-hydrophobic combination with the contact angle set to a combination of 35° and 120°, as shown in fig. 7(b). The initial temperature of the computational domain was 371 K, the heat flux size was 10^6 W/m^2, and both sides were set as periodic boundaries, thus extending the micron-level domain to the generalized domain.

Both wettability schemes have better heat transfer characteristics than the hydrophilic smooth surface (contact angle 35°), and the results are shown in fig. 8. Before 1 ms, both schemes showed the same heat transfer characteristics. However, after 1 ms, Scheme 2 had a lower surface temperature and a higher HTC. This was attributed to the absence of nucleation boiling before 1 ms, resulting in both surfaces having the same heat transfer capacity. After 1 ms, nucleate boiling is formed, and bubbles rapidly accumulate on the hydrophobic surface. This phenomenon creates an upward disturbance force on the bubbles on the hydrophilic surface, causing them to rise rapidly and detach from the wall, thereby improving the heat transfer effect. At 5 ms, it is 380.2 K at the surface of the solid-liquid interface in Scheme 2, and the HTC is 92447 W/m^{2}K. Compared with Scheme 1, the temperature decreased by 0.21%, and the HTC increased by 29.5%. As Scheme 2 showed better heat transfer performance, the structured analysis in the following sections is based on this scheme.

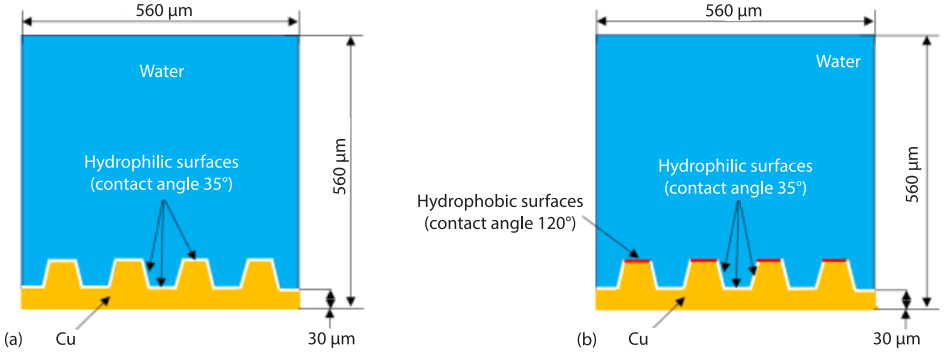

Figure 7. Schematic diagram of two wetting schemes; (a) Scheme 1 and (b) Scheme 2

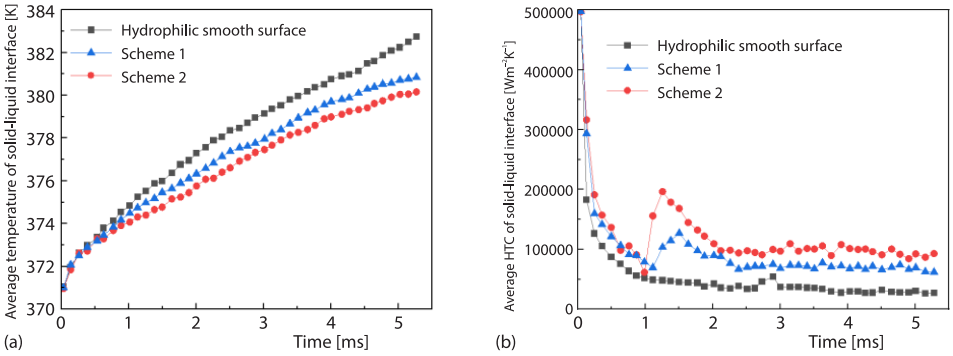

Figure 8. Heat transfer performance of different surfaces; (a) average temperature and (b) average HTC

Figures 9 and 10 present the bubble motion *vs.* velocity vector plots for the two wettability schemes, respectively. By comparing the two figures, it can be observed that for the hydrophilic-hydrophobic composite design scheme, the diameter of the detached bubble from its hydrophilic surface at the bottom is smaller and the rising speed is faster. At 5.1 ms, the upward velocity of the bubble is 2.5 m/s, which is 35% higher than that of the hydrophilic trapezoidal raised surface.

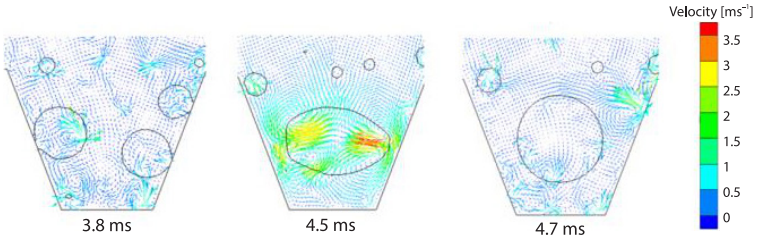

Figure 9. Vector diagram of bubble motion and velocity on the hydrophilic surface

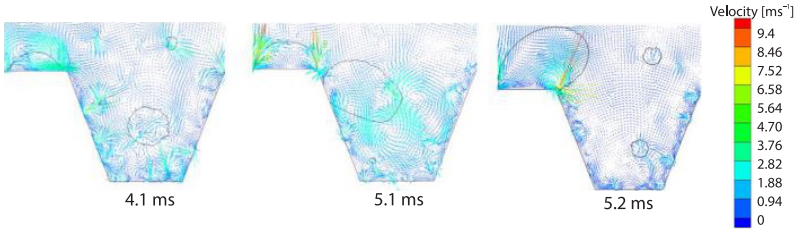

Figure 10. Vector diagram of bubble motion and velocity on the combined hydrophilic-hydrophobic surface

Optimization solution and result analysis

The structural parameters of micro-structured surfaces have a significant impact on heat transfer capacity, so they are used as optimization variables to analyze their influence on heat transfer capacity. The specific variation range is presented in tab. 4. The values in the table are chosen without changing the size of the computational domain, the number and arrangement of the trapezoidal raised in the computational domain.

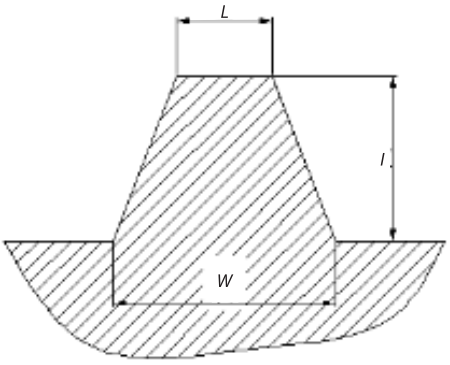

Figure 11. Variable location diagram

Table 4. Optimization of the range of values of variables

Variables	The lower limit of value	The upper limit of value
L [μm]	20	60
W [μm]	50	100
H [μm]	30	100

Design of sample

This paper uses the Latin hypercube sampling method to design sample plans with different optimization variables [19]. The minimum number of sampling points required is determined by the following equation.

$$S \geq \frac{(N+1)(N+2)}{2} \tag{10}$$

where S is the number of points sampled and N – the number of selected structural variables.

A total of 10 sets of sampling points were taken for this sampling as shown in tab. 5. Among them, ΔT is the maximum average temperature rise, and HTC is the average heat transfer coefficient.

Table 5. Sampling point scheme and calculation results

Factor	Sampling point scheme			Calculation results	
	L [μm]	W [μm]	H [μm]	ΔT [K]	HTC [$Wm^{-2}K^{-1}$]
1	20	56	77	10.1	76584.5
2	56	61	30	10.6	74801.6
3	38	83	46	7.9	92526.3
4	42	78	53	7.5	95617.1
5	51	72	100	9.7	82617.7
6	29	89	61	8.7	86877.9
7	47	100	84	9.3	84816.5
8	60	94	92	11.1	72204.1
9	33	67	38	8.1	87488.9
10	24	50	69	11.3	70024.5

Response surface model

The analysis method used in this section is the response surface analysis method. Its core is to obtain the response surface model of the objective and constraint functions using a specific experimental design method and to predict the response values at non-test points [20, 21]. The final response surface approximate model formula is:

$$Z = \varphi_0 + \sum_{i=1}^{N} \varphi_i X_i + \sum_{i} \sum_{j=2}^{N} \varphi_{i,j} X_i X_j + \sum_{i=1}^{N} \varphi_{ii} X_i^2 + \omega \tag{11}$$

where Z is the response approximation, X – the design variable, N – the number of design variables, ω – the random error that obeys normal distribution, and φ – the coefficients to be determined.

The error magnitude between the numerically simulated values and the predicted values from the response surface model is shown in tab. 6. Due to the maximum errors of only 2.68% and 3.08% for HTC and ΔT, respectively, which are extremely small, it is considered that this response surface model can accurately reflect the influence of structural variables on HTC and ΔT.

Table 6. Response surface model accuracy evaluation

Optimization goals	Average error	Maximum error
ΔT	0.89%	1.54%
HTC	2.68%	3.08%

Results analysis

Each structural variable's influence on optimization goals

Figure 12-15 illustrates the analysis of the influence of variations in L, W, and H on HTC and ΔT based on the established response surface model.

Analysis of the effect of structural parameters on the maximum average temperature rise

Figure 12 illustrates the effect trend of L and W on ΔT when H is 65 μm. It is evident from the figure that with the increase of W, ΔT exhibits a trend of initially decreasing and then increasing. This is attributed to the increase in the length of the lower surface, which amplifies the overall heat exchange area, and the increase in bubble nucleation sites, which facilitates an increase in the heat exchange capacity of the micro-structured surface.

The ΔT exhibits different trends with the increase of L for different W conditions, thus the coupling effect of the two should be taken into account. When W is greater than 60 μm, the increase of L reduces the distance between adjacent trapezoidal sides. This facilitates the aggregation and upward floating of bubbles formed on the adjacent sides, thereby enhancing the

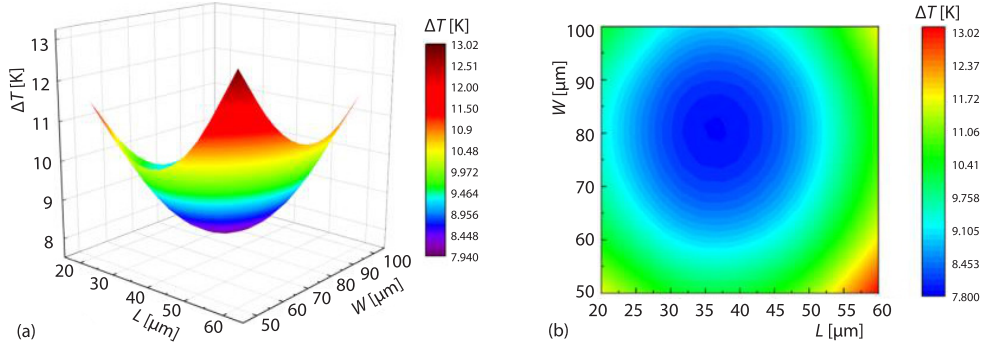

Figure 12. The effect of upper and lower surface length on the maximum average temperature rise; (a) 3-D surface map and (b) 2-D isometric map

heat transfer capacity. Nevertheless, with the further increase of L, the hydrophilic surface area further decreases, leading to a decrease in the heat transfer capacity.

The trend of the effect of L and H on the heat exchange surface ΔT when W is 75 μm is depicted in fig. 13. It can be seen that ΔT decreases and then increases as H increases. This is because when H takes a small value, the distance between the upper and lower surfaces is closer, thus the bubbles formed on the hydrophobic surface will give an upward force to the bubbles on the hydrophilic surface, which accelerates the floating speed, and the frequency of bubble detachment. However, when H takes the minimum value of 30 μm, ΔT does not reach the minimum value. This is because too small a height leads to the formation of film boiling on the hydrophobic surface at the late stage of boiling heat transfer, which deteriorates the heat transfer effect. In the analysis of the coupling effect of H and L, it was observed that L will have an impact on ΔT when H is low, and the magnitude of influence brought by L diminishes significantly with the increase of H.

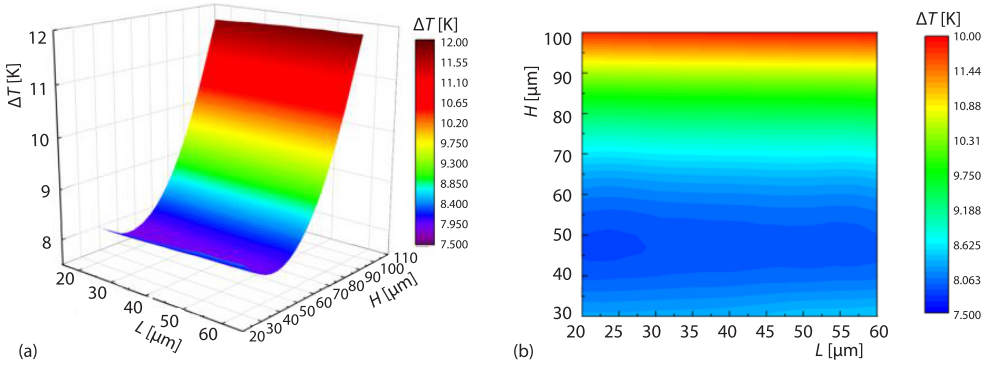

Figure 13. The effect of height and upper surface length on the maximum average temperature rise; (a) 3-D surface map and (b) 2-D isometric map

Analysis of the effect of structural parameters on the average heat transfer coefficient

Figure 14 shows the effect trend of the W and H on the HTC when L is 20 μm. The figure shows that HTC increases and then decreases with increasing H. This is because the perturbation effect brought by the hydrophobic surface is extremely strong when H is small, which accelerates the bubble rise at the beginning of boiling. However, as the boiling process progresses, the hydrophobic surface forms a film boiling over the surface, thus diminishing the heat transfer capacity. Therefore, the value of the maximum HTC is not obtained at the smallest H. When the value of H is large and close to 100 μm, the disturbance effect brought by the hydrophobic surface is very weak. After the bubbles are aggregated, due to the inertial force, the bubbles can hardly float up and show the worst heat transfer performance within 3-6 ms. The HTC tends to increase with the increase of the lower surface length W. This is because the increase of W makes the whole heat exchange area larger, and the number of gasification core points increases, thus increasing the average heat exchange coefficient of the wall surface. Additionally, it can be observed that the H value at the point when HTC attains its maximum value is in the same range as the H value at the minimum average temperature rise, ΔT, in fig. 13.

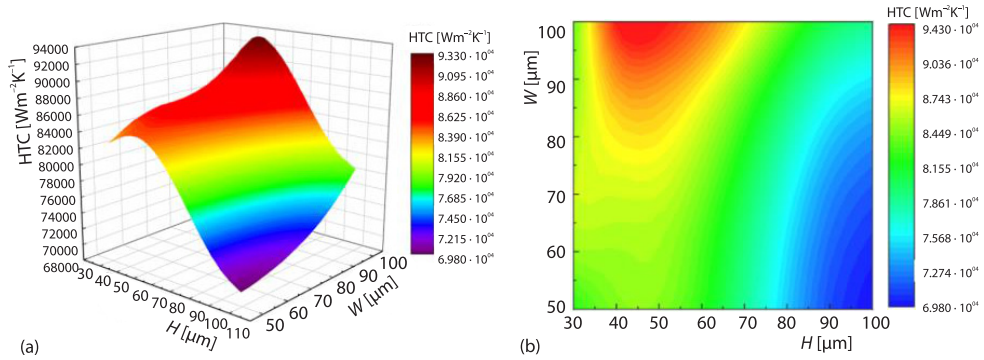

Figure 14. The effect of height and lower surface length on the average HTC; (a) 3-D surface map and (b) 2-D isometric map

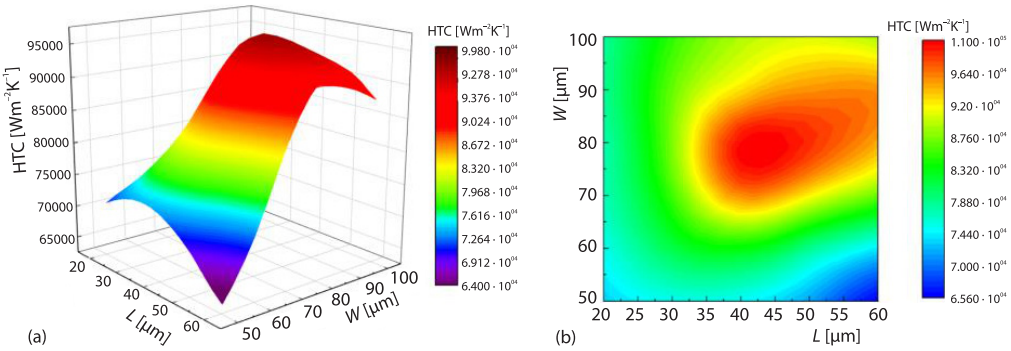

Figure 15. The effect of upper and lower surface length on the average HTC; (a) 3-D surface map and (b) 2-D isometric map

The trend of the effect of L and W on HTC when H is taken as 45 μm is shown in fig. 15. The figure shows that HTC shows a trend of increasing and then decreasing as L and W increase. This is because the L makes the hydrophobic surface area increase, which strengthens the aggregation and disturbance of bubbles on the hydrophobic surface. However, the formation of film boiling in the later stage deteriorates the heat transfer performance. Increasing W enlarges the heat transfer area on the hydrophilic surface, leading to the formation of more nucleation sites during the pre-boiling heat transfer stage, which enhances the heat transfer. However, as W continues to become larger, the bubbles formed on the side walls of adjacent micro-structures weaken the perturbation effect between each other, the frequency of bubble uplifting decreases, and the heat transfer capacity decreases.

Contribution rate analysis of each parameter

The ANOVA (analysis of variance) method was used in this section analyze the variance contribution of L, W, and H to HTC and ΔT [22]. This is shown in fig. 16, H has the largest proportion in the contribution rate of HTC and ΔT, which are 51.7% and 56.7%,

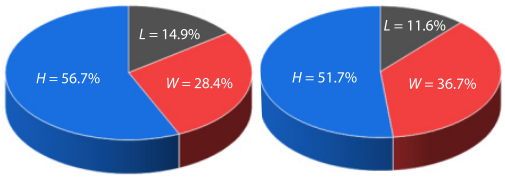

Figure 16. Contribution of each structural parameter to the optimization objective; (a) maximum average temperature rise and (b) average heat transfer coefficient

respectively. This indicates that H is among the most influential structural parameters. The L exhibits the least contribution the optimization targets HTC and ΔT, which are 11.6% and 14.9%, respectively. This suggests that more attention should be paid to the effects of H and W when analyzing the heat transfer characteristics of truncated cone-shaped surfaces.

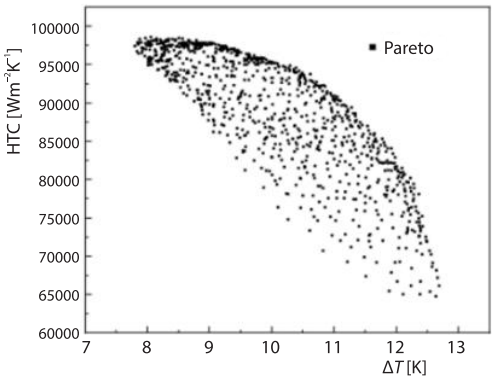

Figure 17. The 2-D Pareto solution frontiers

Multi-objective optimization results analysis

In this paper, the optimal solution of the requested optimization function and the corresponding values of the optimization variables are found in Insight software using the modified NSGA-II algorithm of the genetic algorithm proposed by Deb *et al.* [23]. Figure 17 shows the 2-D Pareto solution set frontier resulting from the NSGA-II algorithm.

After comparing and analyzing the results for each optimization objective, the finalized optimization variable schemes and their corresponding optimized objective response values are shown in tab. 7. The optimization results show a 33.9% reduction in ΔT and a 194.5% increase in HTC compared to the hydrophilic smooth surface.

Table 7. Optimization scheme results compared with simulation values

Factors	Hydrophilic smooth surface	Optimization Results			Improvement [%]
		Optimal solution model	Simulation verification model	Response value error [%]	
L [μm]		41.2	41.2		
W [μm]		82.8	82.8		
H [μm]		50.6	50.6		
HTC [$Wm^{-2}K^{-1}$]	32793.8	97905.5	96569.6	1.36%	+194.5%
ΔT [K]	11.8	7.8	7.9	0.85%	–33.9%

Conclusions

This study established a numerical calculation model based on pool boiling experiments, and used this model to perform numerical simulations on different wettability schemes of micro-structured surfaces with trapezoidal raised. A response surface model was established with the structural parameters L, W, and H as independent variables and HTC and ΔT as optimization objectives, and the influence of each structural parameter on the optimization objectives was analyzed. Finally, the optimal optimization solution was derived using a multi-objective optimization method, are as follows.

- In order to shorten the bubble detachment time and increase the rising speed after detachment, a trapezoidal raised surface with a hydrophilic-hydrophobic combination was designed in this study. The results show that the increased hydrophobic surface increases the bubble rise rate on the hydrophilic surface, the bubble detachment diameter becomes smaller, and the heat transfer capacity is enhanced. At 5 ms, the temperature decreased by 0.21%

and the heat transfer coefficient increased by 29.5% compared to the hydrophilic trapezoidal raised surface.

- Using the established response surface model, the method of variance analysis is employed to evaluate the impact of different structural parameters on HTC and ΔT. The results showed that in the contribution of parameters to HTC and ΔT, the influence of H was 51.7% and 56.7%, respectively, while the influence of W was greater than that of L. This indicates that the height of the trapezoidal raised is the most important structural parameter affecting the heat transfer performance.
- The goal of the multi-objective optimization of the micro-structure is to improve the heat transfer capacity. The results indicate that the optimal solution was obtained when the structural parameters were $H = 50.6$ μm, $W = 82.8$ μm, and $L = 41.2$ μm. The average heat transfer coefficient, HTC, is increased by 194.5% and the maximum average temperature rise, ΔT, is reduced by 33.9% compared to a smooth surface.

References

[1] Yuan, X., *et al*., Forecasting the development Trend of Low Emission Vehicle Technologies: Based on Patent Data, *Technological Forecasting and Social Change*, *166* (2021), 120651
[2] Agarwal, A. K., *et al.*, Evolution, Challenges and Path Forward for Low Temperature Combustion Engines, *Progress in Energy and Combustion Science*, *61* (2017), 1
[3] Kalghatgi, G, T., Developments in Internal Combustion Engines and Implications for Combustion Science and Future Transport Fuels, *Proceedings of the Combustion Institute*, *35* (2015), 1, pp. 101-115
[4] Luff, D. C., *et al.*, The Effect of Piston Cooling Jets on Diesel Engine Piston Temperatures, Emissions, and Fuel Consumption, *SAE International Journal of Engines*, *5* (2012), 3, pp. 1300-1311
[5] Razmjooei, B., *et al.*, The Influence of Heat Transfer Due to Radiation Heat Transfer from a Combustion Chamber, *Journal of Thermal Analysis and Calorimetry*, *147* (2021), Feb., pp. 1901-1917
[6] Kang, H., *et al.*, Smart Cooling System of the Double Loop Coolant Structure with Engine Thermal Management Modelling, *Applied Thermal Engineering*, *79* (2015), Mar., pp. 124-131
[7] Chen, X., *et al.*, Study of Different Cooling Structures on the Thermal Status of an Internal Combustion Engine, *Applied Thermal Engineering*, *116* (2017), Apr., pp. 419-432
[8] Yu, Ting., *et al.*, Boiling Heat Transfer and Bubble Distribution on Inhomogeneous Wetting Surface Patterned with Sierpinski Carpet, *Applied Thermal Engineering*, *180* (2020), 115818
[9] Bova S., *et al.*, A Dynamic Nucleate-Boiling Model for CO_2 Reduction in Internal Combustion Engine, *Applied Energy*, *143* (2015), Apr., pp. 271-282
[10] Torregrosa A J., *et al.*, Experiments on Subcooled Flow Boiling in IC Engine-Like Conditions at Low Flow Velocities, *Experimental Thermal and Fluid Science*, *52* (2014), Jan., pp. 347-354
[11] Torregrosa, A. J., *et al.*, A Note on Bubble Sizes in Subcooled Flow Boiling at Low Velocities in Internal Combustion Engine-Like Conditions, *Journal of Applied Fluid Mechanics*, *9* (2016), 5, pp. 2321-2332
[12] Hua, S., *et al*., Numerical Investigation of Two-Phase Flow Characteristics of Subcooled Boiling in IC Engine Cooling Passages Using a New 3-D Two-Fluid Model, *Applied Thermal Engineering*, *90* (2015), Nov., pp. 648-663
[13] Jafari, *et al*., Numerical Simulation of Flow Boiling from an Artificial Cavity in a Micro-Channel, *International Journal of Heat and Mass Transfer*, *97* (2016), June, pp. 270-278
[14] Dong, L., *et al*., An Experimental Investigation of Enhanced Pool Boiling Heat Transfer from Surfaces with Micro/Nanostructures, *International Journal of Heat and Mass Transfer*, *71* 2014), Apr., pp. 189-196
[15] Phan, H. T., *et al.*, Surface Wettability Control by Nanocoating: The Effects on Pool Boiling Heat Transfer and Nucleation Mechanism, *International Journal of Heat and Mass Transfer*, *52* (2009), 23-24, pp. 5459-5471
[16] Betz, A. R., *et al*., Do Surfaces with Mixed Hydrophilic and Hydrophobic Areas Enhance Pool Boiling, *Applied Physics Letters*, *97* (2010), 14, 141909
[17] Li, Q., *et al*., Enhancement of Boiling Heat Transfer Using Hydrophilic-Hydrophobic Mixed Surfaces: A Lattice Boltzmann Study, *Applied Thermal Engineerin*g, *132* (2018), Mar., pp. 490-499
[18] Guo, L., *et al.*, Study on Characteristics of Vapor-Liquid Two-Phase Flow in Mini-Channels, *Nuclear Engineering and Design*, *241* (2011), 10, pp. 4158-4164

[19] Rakhimov, A, C., *et al*., Uncertainty Quantification Method for CFD Validated for Turbulent Mixing Experiments from GEMIX, *Nuclear Engineering and Design*, *358* (2020), 110444
[20] Ganapathy, T., *et al*., Optimization of Performance Parameters of Diesel Engine with Jatropha Biodiesel Using Response Surface Methodology, *International Journal of Solar Energy*, *30* (2011), 1, pp. 76-90
[21] Dong, F., *et al*., Numerical study on Flow and Heat Transfer Performance of Serpentine Parallel Flow Channels in A High-Voltage Heater System, *Thermal Science*, *26* (2022), 1B, pp. 735-752
[22] Jeong, S., *et al*., Data Mining for Aerodynamic Design Space, *Journal of Aerospace Computing, Information, and Communication*, *2* (2005), 11, pp. 452-469
[23] Deb, K., *et al*., *A Fast Elitist Non-Dominated Sorting Genetic Algorithm for Multi-Objective Optimization: NSGA-II, Parallel Problem Solving from Nature*, Springer, Berlin, Heidelberg, Germany, 2000, pp. 849-858

Paper submitted: February 25, 2023
Paper revised: April 13, 2023
Paper accepted: April 20, 2023